metals

MDPI

Article

Pre-Aging Prior to Delayed Artificial Aging Modulates Precipitation Behavior and Strengthening Response in an Al-Mg-Si-Cu Alloy

Qingyong Zheng [1,2], Huixue Jiang [1], Yuxing Tian [1], Guanmei Niu [1], Mingchao Yu [1], Xiaobin Guo [2], Zhihao Zhao [3], Gaowu Qin [3,4] and Hutian Li [1,*]

[1] Chinalco Materials Application Research Institute Co., Ltd., Beijing 102209, China
[2] School of Materials Science and Engineering, Central South University, Changsha 410083, China
[3] School of Materials Science and Engineering, Northeastern University, Shenyang 110819, China
[4] Institute for Strategy Materials and Components, Shenyang University of Chemical Technology, Shenyang 110142, China
* Correspondence: hutian_li@126.com

Abstract

Room-temperature storage after solution treatment and quenching is often unavoidable during the industrial processing of Al-Mg-Si-Cu alloys, but its interaction with pre-aging and the subsequent artificial aging response remains insufficiently quantified. Here, we demonstrate a pre-aging-assisted delayed artificial aging strategy to regulate β″/L precipitation and improve the strengthening response of an Al-Mg-Si-Cu alloy after short-term room-temperature storage. After solution treatment and quenching, the alloy was stored at room temperature for 6–48 h with or without prior pre-aging at 120 °C, followed by artificial aging at 170 °C. It is found that both the delayed artificial aging (DA) and pre-aging-assisted delayed artificial aging (PDA) routes show limited sensitivity to room-temperature storage time within 6–48 h, whereas PDA consistently increases the yield strength and ultimate tensile strength by approximately 10 MPa compared with the corresponding DA route, with a slight reduction in elongation. Based on Avrami–Johnson–Mehl analysis, the activation energy for β″ precipitation decreases from 102.74 kJ/mol in the DA-pre state and 107.13 kJ/mol in the solution-treated state to 70.63 kJ/mol in the PDA-pre state, indicating that pre-aging modifies the initial microstructural state in a manner that facilitates subsequent β″ precipitation. Quantitative TEM characterization reveals that PDA has little influence on the average sizes of β″ and L precipitates but increases their number densities. In particular, the number density of β″ precipitates increases by approximately 15% relative to the corresponding DA samples. Strengthening-model calculations further show that β″ precipitates make the dominant contribution to precipitation strengthening, and that the strength improvement under the PDA route mainly originates from the increased β″ number density rather than changes in precipitate size. These results establish a quantitative link between pre-aging, precipitation kinetics, β″/L precipitate population, and strengthening response, providing guidance for optimizing heat-treatment schedules of Al-Mg-Si-Cu extrusion alloys that experience unavoidable room-temperature storage before final artificial aging.

Keywords: Al-Mg-Si-Cu alloy; pre-aging; delayed artificial aging; β″ phase; L phase; precipitation strengthening

Check for updates

Academic Editor: Francesca Borgioli

Received: 9 June 2026
Revised: 18 July 2026
Accepted: 20 July 2026
Published: 3 August 2026

Copyright: © 2026 by the authors. Licensee MDPI, Basel, Switzerland. This article is an open access article distributed under the terms and conditions of the Creative Commons Attribution (CC BY) license.

1. Introduction

Al-Mg-Si-Cu alloys are important lightweight structural materials and have been widely used in new energy vehicles and aerospace industries owing to their good formability, corrosion resistance, and age-hardening capability [1–3]. Compared with conventional Al-Mg-Si alloys, the addition of Cu can further modify the precipitation sequence and promote the formation of Cu-containing metastable phases during artificial aging, thereby improving the strengthening response [4,5]. For precipitation-strengthened aluminum alloys, the mechanical properties are closely associated with the microstructural characteristics of precipitates, including number density, size, morphology, chemical composition, and volume fraction [6–8]. Therefore, controlling the precipitation pathway is essential for obtaining a favorable combination of strength and elongation. Recent work on Al-based functionally graded super-intermetallic compounds has further shown that phase-structure regulation is an important strategy for developing lightweight Al-based materials for demanding structural applications [9].

The precipitation sequence in Al-Mg-Si-Cu alloys is generally described as: SSSS → solute clusters → GP zones → β″, L/S/C, QP, QC→β′, Q′ → β, Q, Si [10–12]. Among these precipitates, β″ is widely regarded as one of the dominant strengthening phases at the peak-aged condition, while Cu-containing metastable phases such as L may also contribute to strengthening depending on alloy composition and aging condition [13,14]. The relative formation of these precipitates is sensitive to solute distribution, vacancy concentration, and the thermal history before artificial aging. Thus, even small changes in the early clustering stage may significantly affect the subsequent precipitation kinetics and final mechanical properties.

Different aging paths have been shown to markedly affect the precipitation behavior of Al-Mg-Si alloys. During natural aging after quenching, solute atoms and quenched-in vacancies can form clusters that are stable at room temperature. However, these clusters are not always effective precursors for β″ precipitation during subsequent artificial aging and may even reduce the age-hardening potential [15,16]. In contrast, low-temperature pre-aging can promote the formation of β″-related precursor clusters with more favorable structural and compositional characteristics, thereby improving the subsequent artificial-aging response [17,18]. Previous studies have demonstrated that natural aging duration, heating strategy and pre-aging can strongly influence clustering behavior, hardening kinetics, and final mechanical properties in Al-Mg-Si alloys [11,19].

In industrial production, solution-treated products may undergo temporary room-temperature storage before final artificial aging [20,21], during which natural aging can alter the initial clustering state and subsequent precipitation response [10,22]. Appropriate pre-aging before natural aging has also been reported to promote stable GP-zones and β″-related precursors, leading to finer and denser age-hardening precipitates during subsequent artificial aging [20,23]. However, for Al-Mg-Si-Cu alloys, the effect of pre-aging before room-temperature storage and final artificial aging remains insufficiently understood, particularly with respect to its influence on subsequent precipitation behavior and strengthening response. In this study, delayed artificial aging (DA) and pre-aging-assisted delayed artificial aging (PDA) routes were designed to evaluate the role of pre-aging in regulating the subsequent precipitation response. After PDA treatment, the apparent activation energy for β″ precipitation was reduced, while the number densities of β″ and L precipitates increased after final artificial aging, leading to an improved strengthening response. A combination of kinetic analysis, quantitative TEM characterization, and strengthening-model calculations was employed to clarify the underlying mechanism.

2. Experimental Material and Methods

An alloy with a chemical composition (wt.%) of Al-0.99Mg-0.98Si-0.7Cu-0.57Mn-0.26Zn-0.12Zr was used in this study, as shown in Table 1. Fe is present at an impurity level of 0.12 wt.%.

Table 1. Chemical composition of the studied Al-Mg-Si-Cu alloy (wt.%).

Elements	Mg	Si	Cu	Mn	Zn	Zr	Fe	Al
Percentage	0.99	0.98	0.7	0.57	0.26	0.12	0.12	Bal.

The alloy was cast, homogenized at 560 °C for 12 h, and subsequently extruded into rods with a diameter of 11.5 mm at an extrusion temperature of 500 °C and an extrusion ratio of 20, with the container, die, and billet temperatures set to 450 °C, 490 °C, and 490 °C, respectively. Prior to aging treatment, the samples were solution-treated at 560 °C for 2 h and water quenched. Then, two different aging paths were applied, as summarized in Figure 1 and Table 2 (RT denotes room-temperature storage at 20 °C): (1) solution treatment at 560 °C followed by water quenching, natural aging at room temperature for a certain period, and then artificial aging at 170 °C; (2) solution treatment at 560 °C followed by water quenching, pre-aging at 120 °C, natural aging at room temperature for a certain period, and subsequently artificial aging at 170 °C.

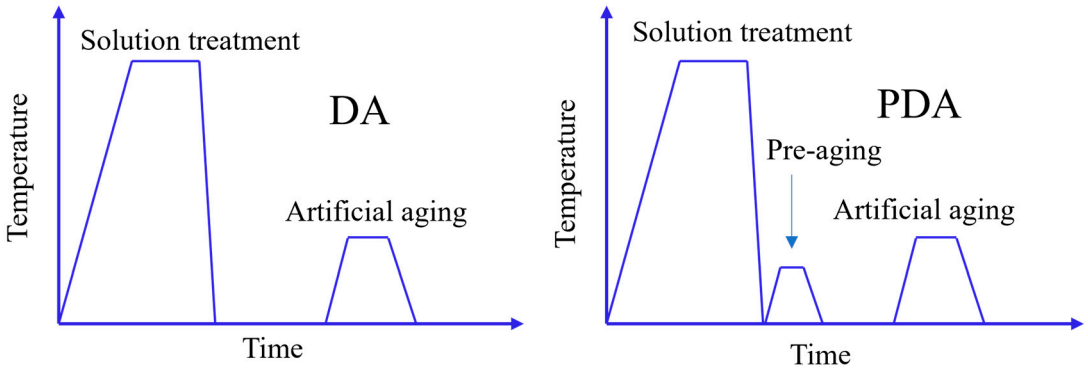


Figure 1. The schematic diagram of the delayed aging (DA) and pre-aging-assisted delayed aging (PDA) routes.

Table 2. Heat-treatment schedules under different aging paths (RT denotes room-temperature storage at 20 °C).

Mark		Treatment
Pre-aging-assisted Delayed Aging (PDA)	P1	120 °C/1 h + RT/6 h + 170 °C/8 h
	P2	120 °C/1 h + RT/24 h + 170 °C/8 h
	P3	120 °C/1 h + RT/48 h + 170 °C/8 h
	T1	120 °C/3 h + RT/24 h + 170 °C/8 h
Delayed Aging (DA)	D1	RT/6 h + 170 °C/8 h
	D2	RT/24 h + 170 °C/8 h
	D3	RT/48 h + 170 °C/8 h

According to previous studies, low-temperature pre-aging in Al-Mg-Si(-Cu) alloys is commonly conducted within a temperature range of approximately 80–120 °C or slightly above 100 °C, which can promote the formation of favorable clusters or β″ precursors and improve the subsequent artificial-aging or bake-hardening response [24,25]. Therefore, the pre-aging temperature of 120 °C used in this work was selected based on previous literature rather than through a separate optimization experiment. This temperature is sufficiently high to promote solute clustering during a short pre-aging treatment, but still lower than

the final artificial-aging temperature of 170 °C, thereby avoiding excessive precipitation before the artificial-aging step.

Vickers hardness measurements were carried out using an MH-500 hardness tester (Shanghai Hengyi Precision Instrument Co., Ltd., Shanghai, China) with an applied load of 200 g and a dwell time of 10 s. For each experimental condition, five indentations were performed at different positions on the sample surface, and the hardness value was reported as the mean ± standard deviation. Tensile specimens were prepared according to GB/T 16865-2023 [26], with an initial gauge length of 25 mm. For each experimental condition, three valid tensile specimens were tested to evaluate the reproducibility of the mechanical properties. The yield strength was determined as the 0.2% proof stress from the engineering stress–strain curve, and the ultimate tensile strength was calculated from the maximum load divided by the original cross-sectional area. The total elongation was obtained from the change in gauge length after fracture. Before testing, the load cell and displacement/extension measurement system of the testing machine were calibrated according to the testing standard. Specimens fractured outside the gauge section were excluded from the statistical analysis. The tensile properties are presented as the mean ± standard deviation, and the corresponding standard deviations are used as error bars in the figures.

DSC measurements were performed using an STA 449 F5 thermal analyzer (NETZSCH-Gerätebau GmbH, Selb, Germany) from room temperature to 620 °C at a heating rate of 10 °C/min. The as-quenched, pre-aged, and peak-aged states were examined to evaluate precipitation and dissolution reactions. For the kinetic analysis of the β″ precipitation peak b, a local linear baseline correction was performed before peak integration. Specifically, the onset and termination temperatures of the peak were determined from the temperatures at which the heat-flow signal deviated from and returned to the surrounding background, respectively. The heat-flow values at these two temperatures were then connected by a straight line, which was taken as the local baseline and subtracted from the experimental curve within the selected temperature interval. The baseline-corrected area from the initial temperature T_0 to a given temperature T was integrated as A(T), and the total corrected peak area was defined as A_f. The transformed fraction was then calculated as $Y(T) = A(T)/A_f$. The integration ranges for the peak were 234–262 °C for the DA-pre and PDA-pre samples and 220–254 °C for the ST sample. The same baseline-selection and integration criteria were applied to all curves to ensure that the fitted apparent activation energies were suitable for relative comparison among the studied conditions.

Electron backscatter diffraction (EBSD) characterization was conducted to analyze the grain-boundary features of the alloy. Prior to EBSD examination, the specimens were sequentially ground using SiC abrasive papers and then mechanically polished. Subsequently, electropolishing was performed in an electrolyte consisting of 10 vol.% $HClO_4$ and 90 vol.% C_2H_5OH at 25 °C under an applied voltage of 30 V for approximately 15 s, in order to obtain a high-quality surface and improve the diffraction pattern quality and spatial resolution of the EBSD measurements. The EBSD analyses were carried out using a JSM-7800F scanning electron microscope (JEOL Ltd., Tokyo, Japan) equipped with an Oxford EBSD detector at an accelerating voltage of 25 kV. The acquired EBSD data were subsequently processed and analyzed using Channel 5 (version 5.12) and AZtecCrystal (version 2.1) software.

The crystal structure, morphology and distribution of the precipitates formed in the alloy were characterized using a JEM-F200 high-resolution transmission electron microscope (HRTEM; JEOL Ltd., Tokyo, Japan). Selected-area diffraction (SAD) was employed to analyze the coarse precipitates. All TEM observations were performed at an accelerating voltage of 200 kV, with the electron beam aligned along the [001] direction of the Al ma-

trix. Thin foils for HRTEM observations were first mechanically ground to a thickness of approximately 100 μm, and subsequently twin-jet electropolished in a solution consisting of 30 vol.% nitric acid and 70 vol.% methanol at a temperature of −25 °C to −30 °C under an applied voltage of 20–30 V.

For quantitative precipitate analysis, the number density and volume fraction of precipitates were geometrically estimated from TEM images. The precipitate number density, N_v, was calculated according to $N_v = N/(At)$, where N is the number of precipitates counted in the analyzed region, A is the corresponding projected area of the TEM image, and t is the local foil thickness. The volume fraction, f, was estimated from the total geometrical volume of the precipitates divided by the analyzed foil volume, i.e., $f = \sum V_i/(At)$, where V_i is the volume of an individual precipitate calculated based on its measured dimensions and assumed morphology. Although the calculated number density and volume fraction are subject to uncertainties associated with two-dimensional projection and geometric idealization, the same imaging conditions, statistical criteria, and calculation procedures were applied to all samples; therefore, the obtained values are considered reliable for comparative analysis of precipitate evolution under different aging paths. In the geometrical calculation, β″ precipitates were treated using an equivalent-size approximation based on their measured projected dimensions, whereas the needle-like L precipitates were approximated as cylindrical particles using their measured diameter and length.

3. Results

3.1. Age Hardening Curve

Figure 2 shows the age-hardening curves under different aging paths: (a) comparison of different room-temperature storage time after quenching; (b) comparison of different pre-aging time after quenching; and (c) comparison of different room-temperature storage time after pre-aging, where the 120 °C/1 h + RT/24 h + 170 °C/8 h treatment exhibited the highest hardness, as consistently shown in all three plots. As shown in Figure 2a, the hardness evolution of the samples stored at room temperature for 6 h, 24 h, and 48 h after quenching exhibits no significant difference, which may be attributed to the relatively short duration of natural aging. Compared with the pre-aged samples, the hardness of the samples in the over-aged condition decreases more noticeably; however, the time required to reach peak aging remains nearly identical for both conditions, at approximately 8 h.

After pre-aging for different durations, the initial hardness is significantly increased, as shown in Figure 2b. The initial hardness of the sample without pre-aging is distinctly lower than that of the pre-aged samples. When the pre-aging time is extended to 3 h, the initial hardness increases markedly from 103.1 HV to 114.0 HV. However, this increase in initial hardness did not lead to improved peak-aged mechanical properties, as shown in Table 3. Therefore, the 3 h pre-aging treatment should not be regarded as more beneficial than the 1 h treatment under the present aging condition. During the over-aging stage, the hardness of the sample without pre-aging decreases rapidly, whereas the pre-aged samples are able to maintain hardness values only slightly lower than the peak hardness. This behavior indicates that pre-aging contributes to improved stability during the over-aging stage. As shown in Figure 2c, the pre-aged samples exhibit good stability even after subsequent room-temperature storage. Pre-aged samples stored at room temperature for 6 h, 24 h, and 48 h show little difference in the subsequent artificial aging response. The pre-aged samples demonstrate superior performance compared with the samples without pre-aging, in terms of both peak hardness and over-aging stability. The alloy investigated in this study contains excess Si and a relatively high Cu content, which can accelerate the age-hardening response [4,5]. The influence of room-temperature storage on subsequent artificial aging is generally weaker in high-Cu alloys.

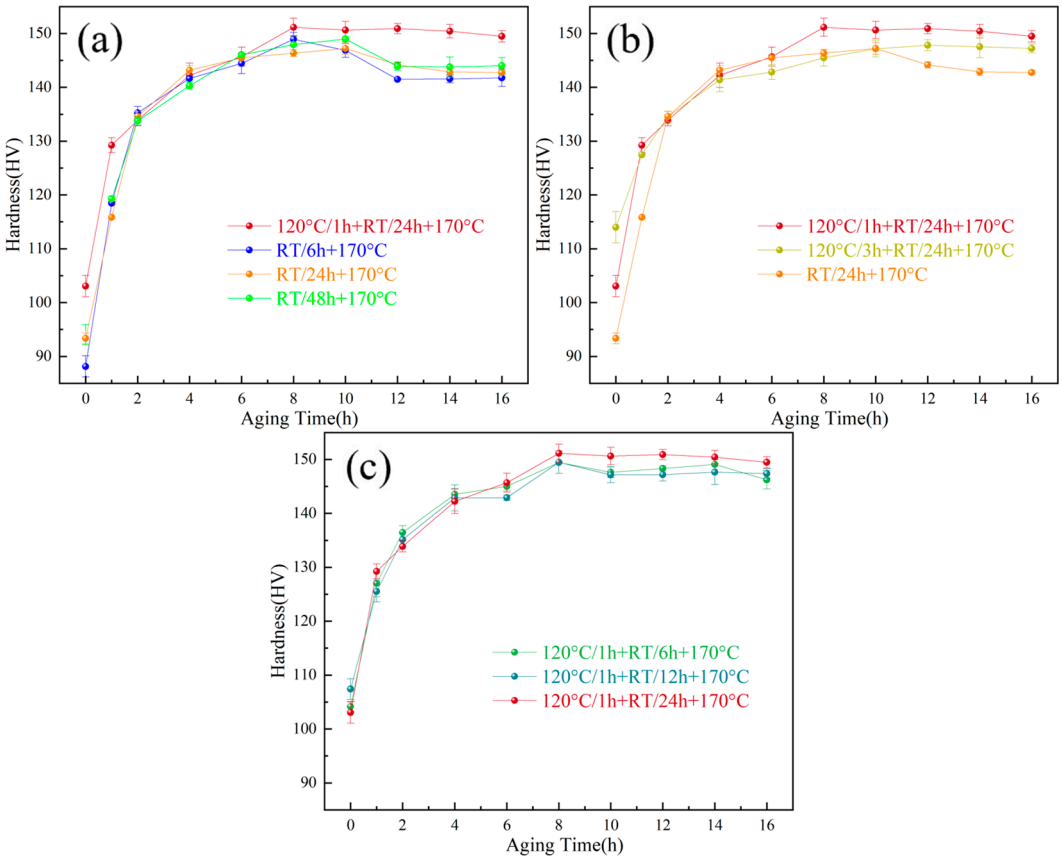


Figure 2. Age-hardening curves under different aging paths: (**a**) comparison of different natural aging times after quenching; (**b**) comparison of different pre-aging times after quenching; (**c**) comparison of different natural aging times after pre-aging.

Table 3. Mechanical properties of the alloy under different treatment conditions.

Samples	Yield Strength (MPa)	Tensile Strength (MPa)	Elongation (%)
P1	330 ± 2	413 ± 4	21.3 ± 0.2
P2	334 ± 6	416 ± 7	22.2 ± 0.2
P3	333 ± 5	415 ± 7	22.3 ± 0.2
T1	328 ± 3	412 ± 4	21.4 ± 0.3
D1	322 ± 4	403 ± 4	22.0 ± 0.2
D2	324 ± 5	404 ± 5	22.9 ± 0.2
D3	323 ± 4	406 ± 5	23.1 ± 0.2

3.2. Mechanical Properties

The mechanical properties of the samples subjected to different aging paths are presented in Figure 3 and Table 3. Compared with the corresponding DA samples with the same room-temperature storage time, the PDA samples consistently exhibit slightly higher yield strength and ultimate tensile strength, with an improvement of approximately 10 MPa, whereas the elongation is slightly reduced. Since the strength difference between the PDA and DA routes is generally larger than the standard deviation range obtained from repeated tensile tests, this modest strength improvement can be considered to have good experimental reliability rather than being caused by experimental scatter. In contrast, for both the DA and PDA routes, neither the yield strength nor the ultimate tensile strength shows a clear increasing trend with increasing room-temperature storage time, indicating that the mechanical properties are relatively insensitive to short-term room-temperature storage within the range examined in this study. The overall higher strength of the PDA

samples suggests that pre-aging at 120 °C provides a more effective precipitation pathway during subsequent artificial aging.

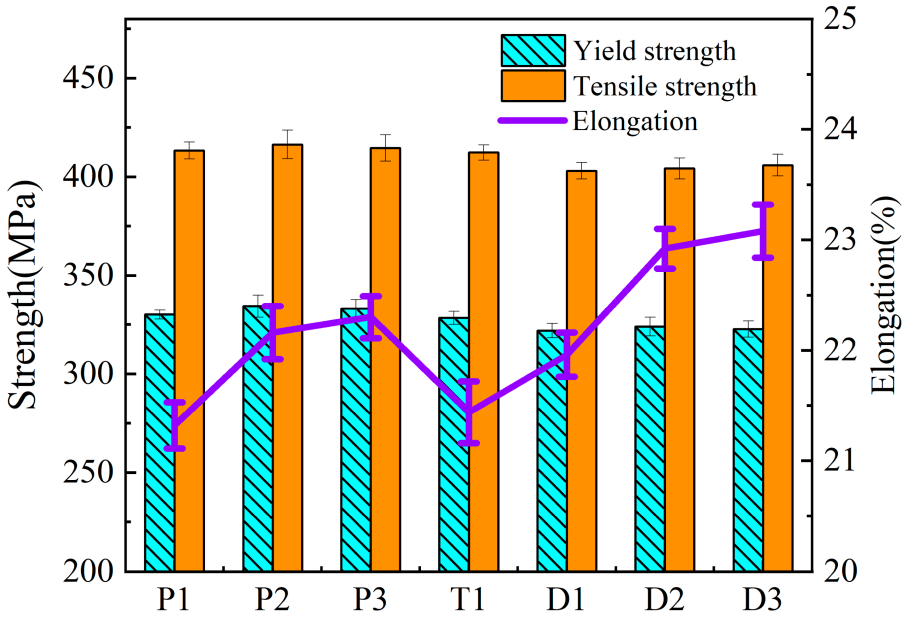


Figure 3. Mechanical properties of different aging paths.

When the pre-aging time was extended to 3 h, both strength and elongation decreased compared with the 120 °C/1 h condition, indicating that excessive pre-aging is not beneficial under the present aging condition. This phenomenon may be related to the overdevelopment of solute clusters or β″-related precursors during the pre-aging stage. Previous studies have shown that the type, size, number density, and thermal stability of clusters formed during pre-aging strongly influence subsequent β″ precipitation. Properly formed GP zones or precursor clusters can act as effective nucleation sites for β″ precipitates, whereas not all clusters are equally favorable for β″ precipitation [27]. In addition, the optimization of pre-aging temperature and holding time in AA6022 alloy has shown that a longer pre-aging time does not necessarily result in a better subsequent hardening response [24]. Therefore, while an appropriate short-time pre-aging treatment can promote the formation of favorable clusters or β″ precursors, extending the pre-aging time may lead to coarsening or stabilization of these precursors and may also consume part of the supersaturated solute atoms and quenched-in vacancies before final artificial aging. As a result, the subsequent nucleation density of fine β″ precipitates may not further increase, and the precipitation-strengthening potential during final aging can be reduced. Therefore, the 120 °C/1 h pre-aging treatment appears to provide a more suitable precursor state for the subsequent PDA process than the longer 120 °C/3 h treatment.

3.3. DSC Curves

Figure 4 presents the DSC curves of the solution-treated and quenched sample (ST), the naturally aged state at room temperature (DA-pre) and the pre-aged state before artificial aging at 170 °C (PDA-pre), and the peak-aged states (DA-peak and PDA-peak). One endothermic peak, denoted as peak a, and two exothermic peaks, denoted as peaks b and c, can be identified. Peak a is attributed to the dissolution of GP zones or solute clusters formed before or during the early stage of DSC heating [28]. The exothermic peaks are associated with precipitation reactions during non-isothermal heating. In Al-Mg-Si-Cu alloys, several metastable and equilibrium precipitates may form during artificial aging, including β″, β′, L, Q′, and Q phases. The β″ phase is generally regarded as the dominant

strengthening precipitate at the peak-aged condition because of its high number density, fine size, and coherent or semi-coherent relationship with the Al matrix. Therefore, peak b is assigned to β″ precipitation. The β′ phase is a coarser post-β″ metastable precipitate that usually forms at higher aging temperatures or during over-aging. In Cu-containing Al-Mg-Si alloys, Cu-containing metastable precipitates such as L and Q′ may also form. The L phase is closely related to the Q′/Q precipitation sequence and is commonly regarded as a precursor or related variant of Q′, whereas Q is the equilibrium Al-Cu-Mg-Si phase with a composition close to $Al_3Cu_2Mg_9Si_7$. Therefore, peak c is attributed to overlapping precipitation reactions involving β′/L/Q′-related phases rather than a single isolated phase transformation [29].

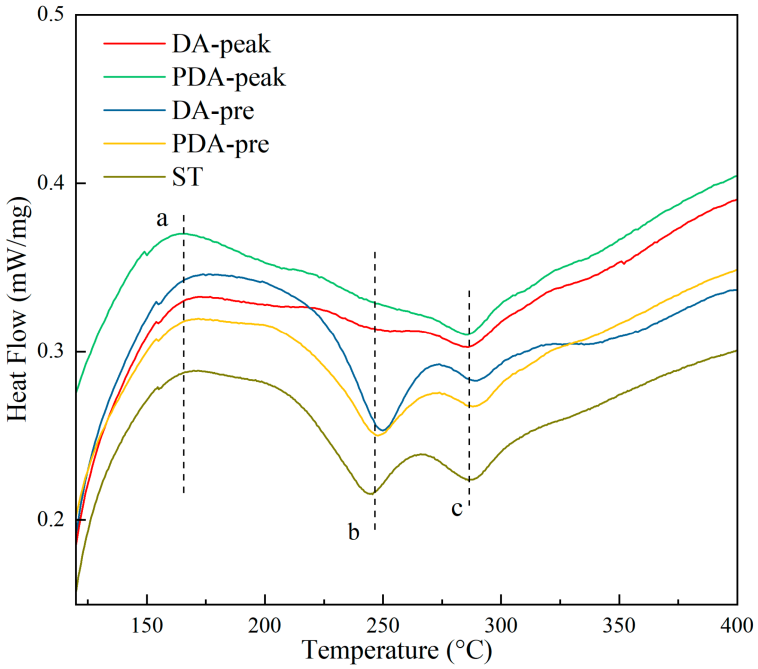


Figure 4. Calorimetric analysis of the pre-aged, peak-aged, and solution-treated Al-Mg-Si-Cu alloy.

In the present work, peak b is clearly observed in the ST, DA-pre, and PDA-pre states, but disappears in the DA-peak and PDA-peak states. This peak evolution supports the assignment of peak b to β″ precipitation. For the peak-aged samples, a sufficient amount of β″ precipitates has already formed during aging at 170 °C. Therefore, during subsequent DSC heating, the existing β″ precipitates are more likely to transform into more stable phases rather than form again, and no distinct β″-related exothermic peak is detected. In contrast, in the ST, DA-pre, and PDA-pre states, β″ precipitation has not been fully completed before DSC heating. Consequently, part of the solute clusters or GP zones can transform into β″ during the non-isothermal heating process, giving rise to the exothermic peak b.

Among the three conditions exhibiting peak b, the peak area of PDA-pre is relatively smaller than those of the other two conditions. This suggests that the pre-treatment at 120 °C for 1 h may have induced the formation of a small amount of β″ precipitates, thereby reducing the amount of β″ that can form during the DSC experiment and consequently decreasing the exothermic peak area. Similarly, the peak-aged PDA and DA samples show a smaller peak c area compared with the corresponding PDA-pre and DA-pre conditions, which can be attributed to the prior formation of strengthening precipitates that consume solute atoms, leading to a reduced heat release during subsequent precipitation reactions [28]. Furthermore, the comparable peak c areas of the PDA-pre, DA-pre, and ST

samples suggest that the heat release associated with the subsequent high-temperature precipitation reactions is similar among these conditions.

3.4. TEM Quantitative Analysis of Strengthening Phases

Figure 5 shows bright-field TEM images of samples subjected to room-temperature storage after solution quenching and subsequent peak aging: (a, b) RT/6 h; (c, d) RT/6 h + 170 °C/8 h; and (e, f) RT/24 h + 170 °C/8 h. After RT/6 h storage before artificial aging, no clearly discernible precipitates were observed, while only weak nanoscale contrast fluctuations were present in the matrix, which may be associated with early-stage solute clustering. These clusters or GP zones do not contribute directly to strengthening, resulting in a relatively low hardness, which is consistent with the lower initial hardness shown in Figure 2a. Nevertheless, such cluster-related nanoscale contrast features may act as effective nucleation sites for precipitates during subsequent aging, thereby increasing precipitate number density and enhancing the alloy strength [8].

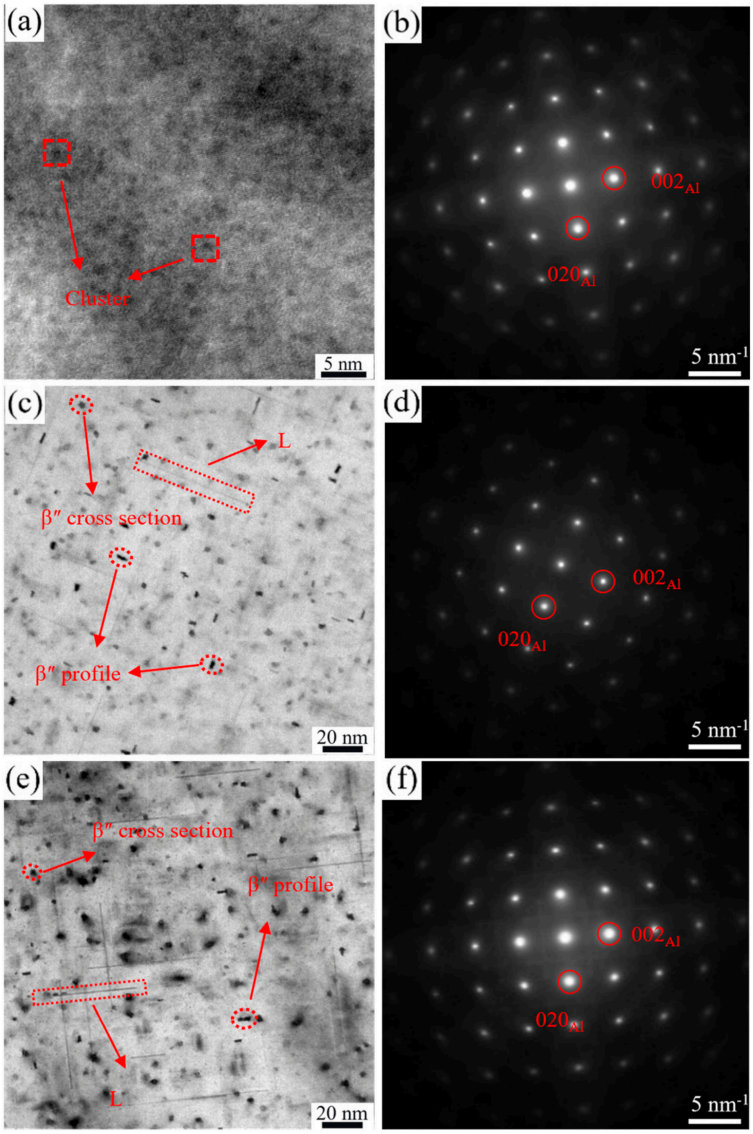


Figure 5. Bright-field TEM images and corresponding diffraction patterns after solution treatment and quenching followed by natural aging at room temperature and peak aging (DA): (**a**,**b**) RT/6 h; (**c**,**d**) RT/6 h + 170 °C/8 h; (**e**,**f**) RT/24 h + 170 °C/8 h.

As shown in Figure 5c,e, two main types of precipitates can be identified in the peak-aged condition: (1) β″ precipitates exhibiting irregular cross-sectional morphologies and block-like appearances in longitudinal sections [7]; and (2) relatively long, needle-shaped L-phase precipitates [30]. The corresponding high-resolution TEM images are presented in Figure 6. As shown in Figure 6b,c, the fast Fourier transform (FFT) patterns are consistent with the diffraction characteristics of the β″ phase, confirming their identification as β″ precipitates. The lattice parameters of the β″ phase are a = 1.521 nm, c = 0.674 nm, and β = 105.3°, and the orientation relationship with the Al matrix can be described as $(40\bar{3})_{\beta''}//(002)_{Al}$ and $(601)_{\beta''}//(020)_{Al}$ [4]. The needle-shaped L-phase precipitates are generally considered to be precursors of the Q′ phase and exhibit a high degree of coherency with the Al matrix [30].

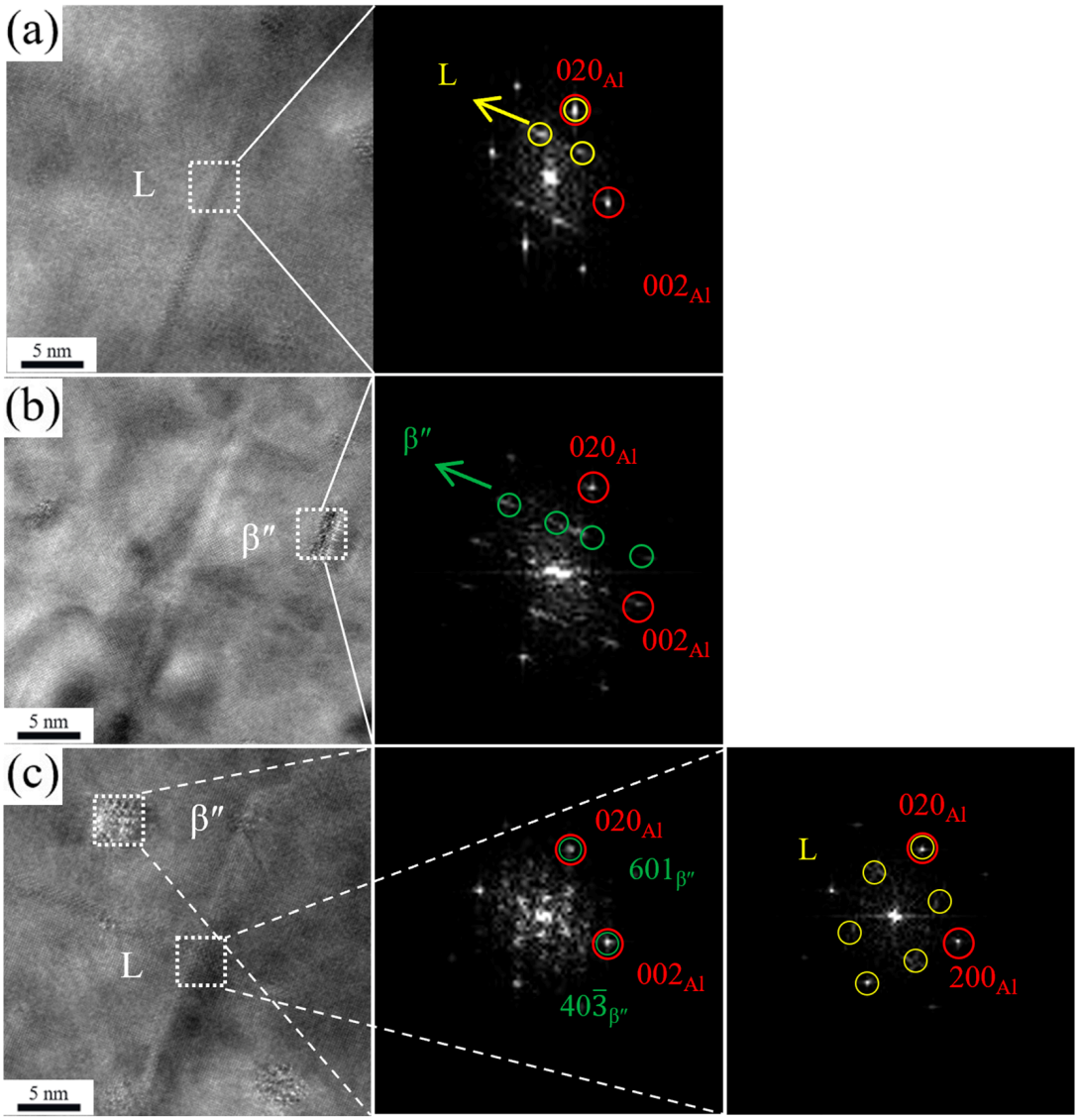


Figure 6. HRTEM images and corresponding diffraction patterns of β″ and L phases under the DA path: (**a**) L phase; (**b**) β″ phase; (**c**) coexisting β″ and L phases.

Table 4 summarizes the measured size, number density, and volume fraction of β″ and L precipitates under different aging paths. For the DA route, extending the room-temperature holding time after solution quenching does not result in any pronounced changes in the size or number density of either β″ or L precipitates, indicating that short-term natural aging after quenching has a negligible influence on the precipitation behavior

during subsequent DA treatment. In contrast to the DA condition, the PDA route leads to a slight increase in the number density and volume fraction of both β″ and L precipitates, while their average sizes remain essentially unchanged.

During the PDA process, the pre-aging treatment at 120 °C does not induce the formation of clearly discernible precipitates in the matrix; instead, a large number of weak nanoscale contrast fluctuations are still present. Meanwhile, faint cross-shaped diffraction streaks can be observed in the corresponding diffraction patterns, indicating the formation of a small amount of β″ precipitates in the matrix [4], as shown in Figure 7b. These nanoscale contrast features may be associated with precursor clusters related to subsequent β″ and L precipitation during aging at 170 °C.

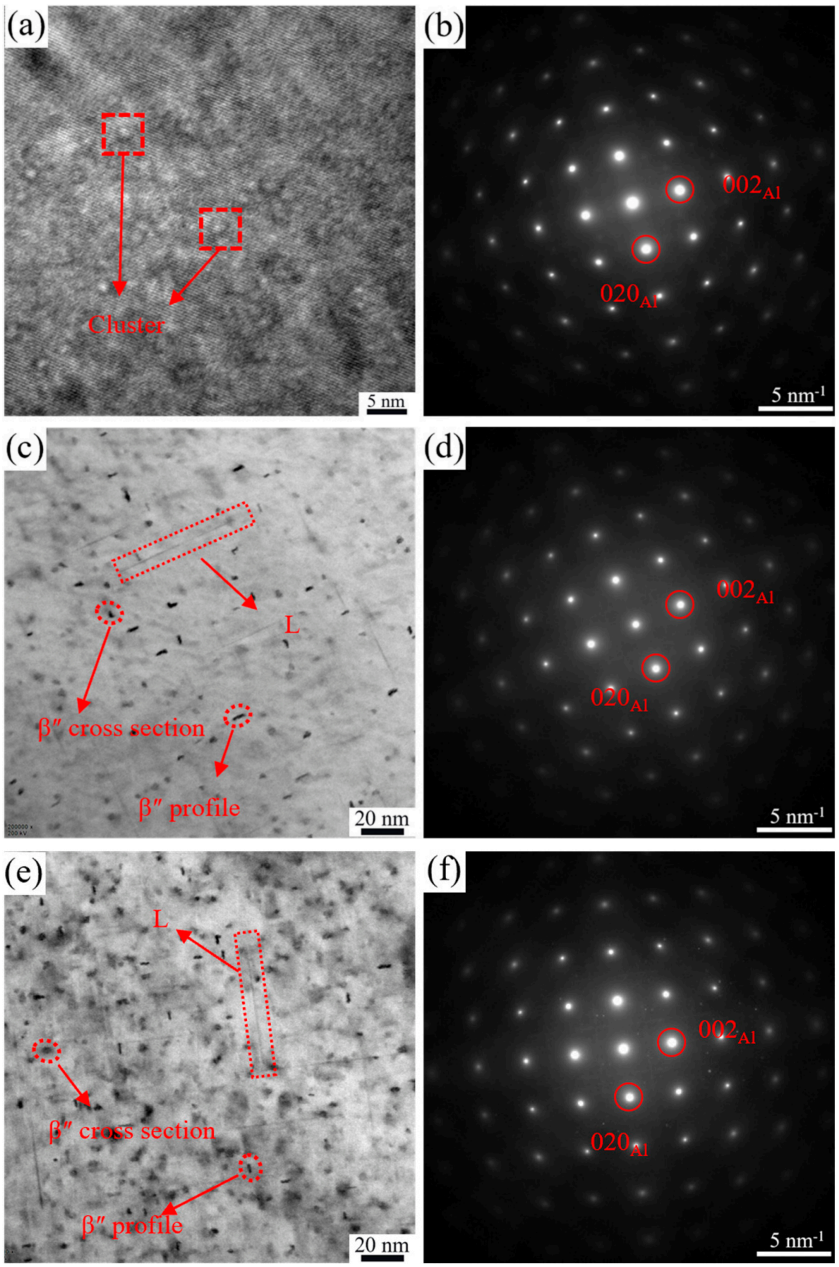


Figure 7. Bright-field TEM images and the corresponding diffraction patterns after solution treatment and quenching followed by pre-aging, room temperature storage and peak aging (PDA): (**a**,**b**) 120 °C/1 h + RT/6 h; (**c**,**d**) 120 °C/1 h + RT/6 h + 170 °C/8 h; (**e**,**f**) 120 °C/1 h + RT/24 h + 170 °C/8 h.

Table 4. Quantitative statistics of precipitates under different aging conditions.

	Parameters	D1	P1	D2	P2
Rod β″	Equivalent diameter (nm)	2.57	2.60	2.58	2.63
	Number density (nm^{-3})	7.07×10^{-5}	8.03×10^{-5}	7.36×10^{-5}	8.50×10^{-5}
	Volume fraction (%)	1.17	1.29	1.19	1.36
Acicular L	Diameter (nm)	0.99	0.96	0.99	0.97
	Length (nm)	42.8	44.1	46.0	45.0
	Number density (nm^{-3})	4.74×10^{-5}	5.35×10^{-5}	4.92×10^{-5}	5.53×10^{-5}
	Volume fraction (%)	0.64	0.69	0.66	0.69

Regardless of whether the PDA or DA route is applied, the number density of β″ precipitates is significantly higher than that of L precipitates, and their corresponding volume fraction is also greater. Consequently, β″ precipitates play the dominant role in precipitation strengthening in the present alloy. From a mechanistic perspective, β″ precipitates are generally regarded as shearable obstacles to dislocation motion, whereas L precipitates are typically considered non-shearable [10]. The corresponding strengthening calculations based on these two mechanisms are presented and discussed in the following section.

Figures 7 and 8 present bright-field TEM images and high-resolution images of precipitates in samples subjected to aging after pre-aging followed by room-temperature holding for different durations. For the PDA route, extending the room-temperature holding time after pre-aging does not lead to any significant changes in the number density or volume fraction of precipitates. This observation is consistent with the mechanical property results shown in Figure 3 and indicates that pre-aging effectively enhances the microstructural stability of the alloy during subsequent room-temperature holding.

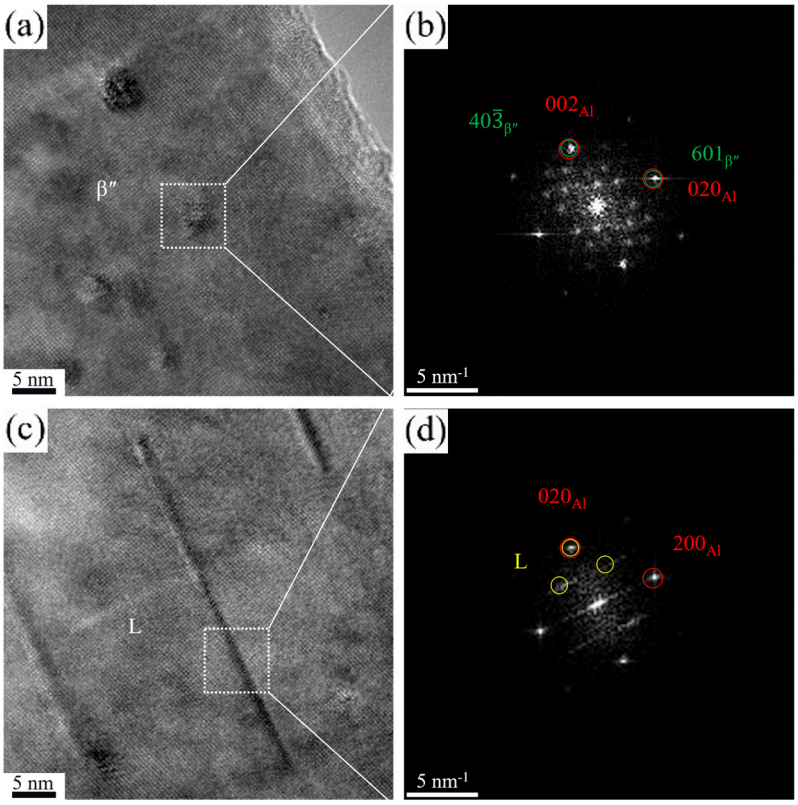


Figure 8. HRTEM images and corresponding diffraction patterns of β″ and L phases under the PDA path: (**a**,**c**) HRTEM images of the β″ and L phases, respectively; (**b**,**d**) corresponding diffraction patterns of the β″ and L phases, respectively.

Although both DA and PDA routes exhibit a relatively low sensitivity to room-temperature holding time, as reflected in Figure 3 and Table 4, the underlying mechanisms are fundamentally different. In the DA route, room-temperature holding after quenching is essentially equivalent to a period of natural aging.

During this process, decomposition of the supersaturated solid solution leads to the formation of a large number of low-temperature-stable solute clusters, thereby reducing the precipitation strengthening potential during subsequent artificial aging [11]. Since the detrimental effects of natural aging on mechanical properties generally manifest over relatively long timescales, short holding periods on the order of several hours or even tens of hours do not result in pronounced differences in mechanical performance.

It should be noted that the number density and volume fraction reported here are geometrically estimated values derived from TEM statistics rather than absolute three-dimensional measurements. Nevertheless, because all conditions were analyzed using an identical statistical protocol, these data provide a meaningful basis for comparing the relative changes in precipitate population induced by different aging paths.

Figure 9 shows quantitative statistical results based on measurements of at least 400 precipitates for each condition. The data indicate that the average measured size of L precipitates does not vary significantly among different aging conditions, suggesting that the performance differences between the two aging routes mainly originate from variations in precipitate number density rather than precipitate size. Specifically, the precipitate number density obtained via the PDA route is higher than that achieved through the DA route, further demonstrating that PDA enhances the mechanical properties of the alloy by increasing the density of effective nucleation sites for precipitate formation.

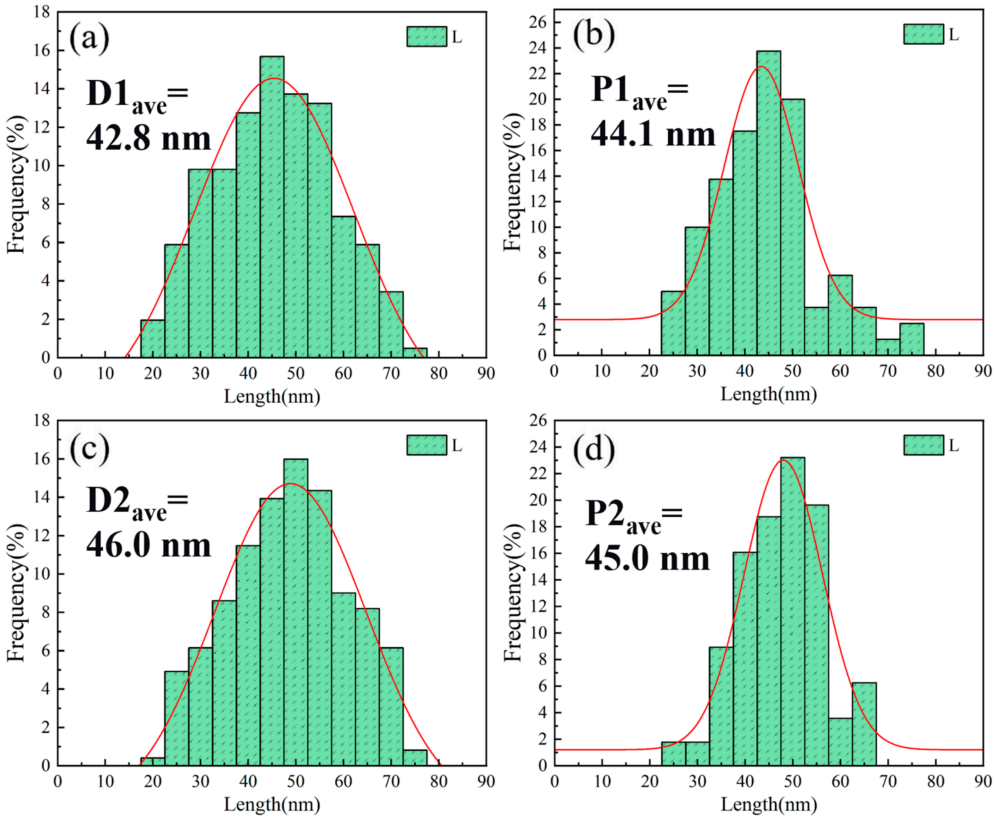


Figure 9. Size-distribution histograms of L phase in the TEM microstructures of peak aging conditions: (**a**) D1; (**b**) P1; (**c**) D2; (**d**) P2.

It is worth noting that the size distribution of L precipitates in the P2 condition is narrower than those in the other conditions, as shown in Figure 9d. This may indicate that the nucleation and growth of L precipitates become more uniform after the 120 °C/1 h pre-aging treatment followed by 24 h room-temperature storage. The precursor clusters formed during pre-aging may provide relatively uniform nucleation sites during subsequent artificial aging, thereby reducing the growth difference among individual L precipitates. However, TEM-based size statistics are inherently local and may be influenced by the selected observation area, local microstructural heterogeneity, projection effects, and statistical fluctuations. Therefore, the narrower distribution in Figure 9d should be regarded as a possible indication of more uniform precipitation in the P2 condition, rather than definitive evidence of a fundamentally different growth mechanism.

4. Discussion

4.1. Precipitation Kinetics of Different Aging Paths

The precipitation kinetics during the non-isothermal aging process shown in Figure 4 can be quantitatively analyzed using the Avrami–Johnson–Mehl (AJM) equation [31–33], which can be expressed as follows:

$$Y = 1 - exp\left[-(kt)^n\right] \tag{1}$$

$$k = k_0 exp\left(-\frac{Q}{RT}\right) \tag{2}$$

where Y represents the molar volume fraction of precipitates at time t, and k and n are kinetic parameters related to the nucleation density and precipitate growth mode, respectively. For the formation of β″ precipitates, the Avrami exponent n is taken as 2, as reported in previous studies [34,35]. The parameter k can be expressed in an Arrhenius form, where k_0 is a constant, Q is the activation energy for precipitation, R is the gas constant with a value of 8.314 J/(mol·K), and T is the absolute temperature.

By differentiating Equation (1), the transformation rate of the precipitate volume fraction during the non-isothermal process can be obtained, as expressed by the following equation:

$$\frac{dY}{dt} = kf(Y) \tag{3}$$

where $f(Y)$ is an implicit function of Y.

By substituting Equation (1) into Equation (3), the following expression can be obtained:

$$f(Y) = n(1-Y)[-ln(1-Y)]^{\frac{n-1}{n}} \tag{4}$$

$$Y = \frac{A(T)}{A_f} \tag{5}$$

where $A(T)$ represents the area under the peak from the initial temperature T_0 to a given temperature T, and A_f denotes the total peak area.

Therefore, the following expression for the transformation rate can be obtained:

$$\frac{dY}{dt} = \left(\frac{dY}{dT}\right)\left(\frac{dT}{dt}\right) = \varphi\left(\frac{dY}{dT}\right) \tag{6}$$

where φ denotes the heating rate. In the present study, φ was set to 10 °C/min.

Based on Equations (2), (4), and (6), the following relationship can be derived:

$$ln\left[\left(\frac{dY}{dT} \times \frac{\varphi}{f(Y)}\right)\right] = lnk_0 - \left(\frac{Q}{R}\right)\left(\frac{1}{T}\right) \tag{7}$$

As can be seen from Equation (7), $ln\left[\left(\frac{dY}{dT} \times \frac{1}{f(Y)}\right)\right]$ exhibits a linear relationship with $\frac{1}{T}$. Accordingly, the activation energy associated with dissolution or precipitation can be determined from the slope and intercept of the corresponding linear fit.

Figure 10 presents the apparent activation energies for β″ precipitation under the three different processing conditions, and the corresponding kinetic parameters are summarized in Table 5. To evaluate the fitting reliability, the coefficients of determination (R^2) were added for the AJM linear fits. The R^2 values for the DA-pre, PDA-pre, and ST samples were 0.98, 0.97, and 0.92, respectively, indicating good linearity within the selected transformation range. The apparent activation energy for β″ precipitation is 70.63 kJ/mol for the PDA-pre sample, which is markedly lower than those of the DA-pre sample and the ST sample, 102.74 and 107.13 kJ/mol, respectively. This result indicates that pre-aging at 120 °C/1 h facilitates subsequent β″ precipitation under the present DSC analysis conditions. Previous studies have reported that pre-aging can promote β″ precipitation and reduce the kinetic barrier for subsequent artificial aging in Al-Mg-Si(-Cu) alloys [22,24,35]. Therefore, the reduced apparent activation energy observed here should not be regarded as a completely new kinetic phenomenon. Instead, DSC-based kinetic analysis was employed as a quantitative tool to compare the precipitation responses of the DA and PDA routes after short-term room-temperature storage. The lower apparent activation energy of the PDA-pre condition suggests that pre-aging provides a more favorable precursor state for subsequent β″ precipitation, which is likely associated with the formation of β″-related precursor clusters during pre-aging.

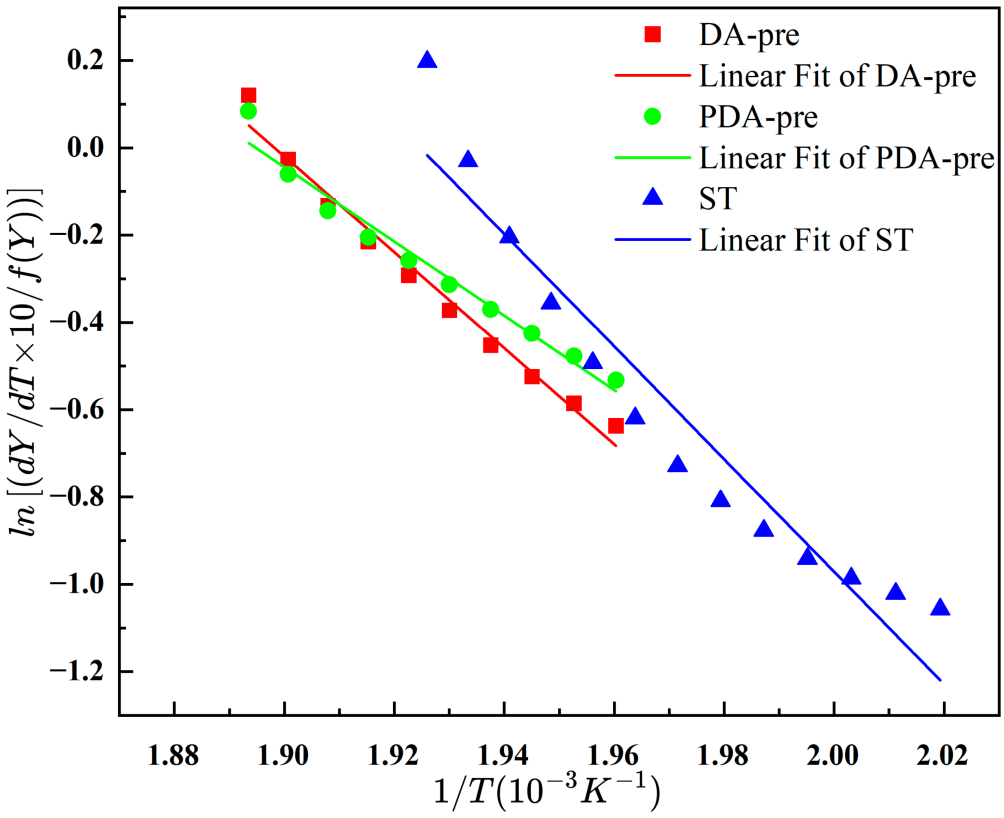


Figure 10. The *ln[dY/dT × 10/f(Y)] − (1/T)* curves of activation energy for the β″ phase transformations in the DA-pre, PDA-pre and ST samples, where 10 represents the corresponding heating rate of 10 °C/min.

Table 5. Kinetic parameters and equations for β″ precipitation under different aging paths.

Sample	Q (kJ/mol)	Kinetic Equation	Coefficient of Determination (R^2)
DA-pre	102.74	$1-exp\left[-2.69\times10^{20}t^2exp(-24,715/T)\right]$	0.98
PDA-pre	70.63	$1-exp\left[-9.64\times10^{13}t^2exp(-16,991/T)\right]$	0.97
ST	107.13	$1-exp\left[-3.55\times10^{21}t^2exp(-25,771/T)\right]$	0.92

The lower apparent activation energy in the PDA-pre condition indicates that the precursor clusters formed during pre-aging can reduce the energy barrier for subsequent β″ precipitation. These clusters may possess local structural or compositional features closer to β″ precipitates, and therefore require less atomic rearrangement to evolve into β″ during artificial aging. Murayama and Hono reported that GP zones formed during low-temperature pre-aging can serve as nucleation sites for β″ precipitates during subsequent artificial aging, whereas clusters formed during natural aging are less effective in this regard [27]. Therefore, pre-aging promotes β″ precipitation by establishing a more favorable initial clustering state, which is reflected by the reduced apparent activation energy and the increased number density of β″ precipitates after final aging.

By comparison, the DA-pre sample, which experienced natural aging at room temperature after solution quenching, shows a slightly reduced apparent activation energy relative to the ST condition. This behavior suggests that short-term natural aging may induce limited solute rearrangement and vacancy-solute interactions, forming a small number of clusters or GP zones that partially assist β″ nucleation during non-isothermal aging. However, their effectiveness appears weaker than that of the precursor clusters formed during the 120 °C pre-aging treatment, resulting in a higher apparent activation energy than that of the PDA-pre sample. It should also be emphasized that the DSC measurements in this study were conducted at a single heating rate of 10 °C/min; therefore, the fitted values should be interpreted as apparent activation energies suitable for relative comparison among the studied conditions rather than absolute activation energies obtained from multi-heating-rate kinetic methods. The activation energy of the L phase could not be directly determined because the L-phase-related reaction overlaps strongly with β′/Q′ precipitation during non-isothermal heating, preventing reliable peak separation and kinetic analysis [36–38].

The difference between the DA-pre and ST samples lies in the thermal history after solution quenching. For the DA-pre sample, 24 h storage at room temperature introduces a short period of natural aging, during which limited solute rearrangement and vacancy-solute interactions may occur. This process can produce a small number of clusters or GP zones that partly assist β″ nucleation during subsequent non-isothermal heating, thereby slightly reducing the apparent activation energy for β″ precipitation [17,21].

The ST sample enters the non-isothermal aging process directly after quenching. During the low-temperature stage of heating, unstable solute clusters or GP zones may form due to the high vacancy concentration. As the temperature increases, part of these clusters or GP zones may dissolve or rearrange before effective β″ precipitation occurs, leading to a higher apparent activation energy for β″ precipitation than that of the DA-pre and PDA-pre conditions [19]. Therefore, the short natural aging treatment in the DA-pre sample modifies the early-stage precipitation pathway, facilitating β″ nucleation and leading to a slightly lower activation energy compared to the ST condition.

4.2. Relationship Between Multiscale Precipitates and Mechanical Properties

The yield strength model was employed to quantify the contributions of different strengthening mechanisms under various aging treatments. The overall yield strength can be expressed as follows [6,39–41]:

$$\sigma_y = \sigma_{ss} + \sigma_{gb} + \sigma_p \tag{8}$$

where σ_{ss}, σ_{gb} and σ_p represent the solid-solution strengthening contribution, the grain boundary strengthening and the precipitation-strengthening contribution of the alloy, respectively. The solid-solution strengthening contribution is calculated according to the following expression [39]:

$$\sigma_{ss} = \sum_j k^j C_i^{j\frac{2}{3}} \tag{9}$$

where σ_{ss} denotes the solid−solution strengthening contribution, k^j is the strengthening coefficient of the j-th solute element, and C_i^j represents the weight concentration of the j-th solute in the matrix. The scaling factors for the solid solution hardening model k^{Si} and k^{Mg} are 66.3 MPa/wt%$^{2/3}$ and 29 MPa/wt%$^{2/3}$ [28].

The grain boundary strengthening of a polycrystalline material is popularly evaluated using the Hall-Petch relation as given below [39]:

$$\sigma_{gb} = \sigma_0 + k_i d^{-\frac{1}{2}} \tag{10}$$

where σ_{gb} is the increase in yield strength due to grain boundary strengthening, σ_0 is the intrinsic strength at infinite grain size, k_i is the locking factor and d is the grain size in microns. Typical values of σ_0 and k_i for Al-alloys are 16 MPa [42] and 0.0065MPa·m$^{1/2}$ [39], respectively.

To determine the grain size of the solution-treated sample, electron backscatter diffraction characterization was performed, and the corresponding results are presented in Figure 11. Based on the EBSD statistical analysis, the average grain size of the solution-treated sample was determined to be 74.3 μm.

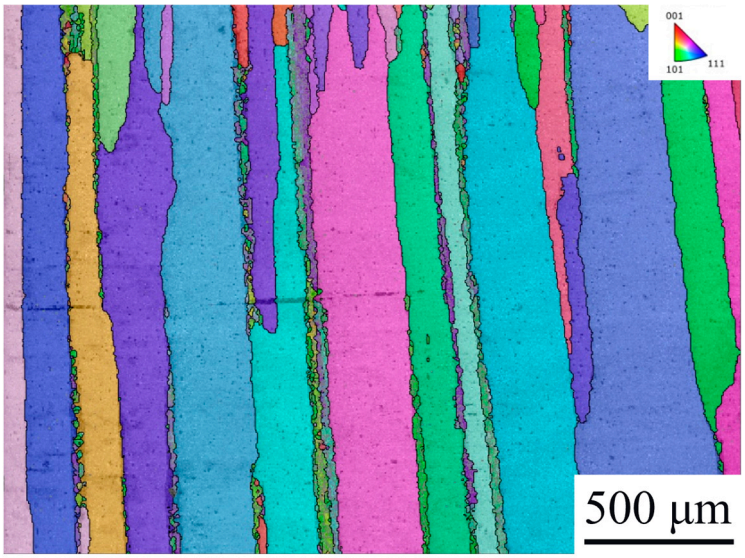


Figure 11. EBSD inverse pole figure (IPF) map obtained from the longitudinal section along the extrusion direction of the solution-treated sample, with an average grain size of 74.3 μm.

Since the β″ and L phases operate via two distinct strengthening mechanisms, with the former following a shearable-precipitate strengthening model and the latter a non-shearable (Orowan-type) strengthening model, the precipitation-strengthening contribution can be calculated as follows:

$$\sigma_p = \sigma_p^{\beta''} + \sigma_p^{L} \tag{11}$$

$$\sigma_p = \frac{M}{br}(2\beta G b^2)^{-\frac{1}{2}} \left(\frac{3f}{2\pi}\right)^{\frac{1}{2}} \overline{F}^{\frac{3}{2}} \tag{12}$$

where M is the Taylor factor, b is the Burger's vector, r is the precipitate radius, β is a constant with a value close to 0.5, G is the shear modulus of the matrix, f is the volume fraction of precipitates, and $\overline{F}$ denotes the average obstacle strength. $\overline{F}$ is a function of the precipitate radius. For weak obstacles, when r is smaller than the critical shearing radius r_c, which is taken as 2.5 nm. In this case, $\overline{F}$ is proportional to the precipitate radius r and can be described by the following expression:

$$\overline{F} = 2\beta G b^2 \frac{r}{r_c} \tag{13}$$

On the other hand, the strong non-shearable particle regime applies when the precipitate radius r exceeds the critical shearing radius r_c, $\overline{F}$ can be expressed as follows:

$$\overline{F} = 2\beta G b^2 \tag{14}$$

Based on the size, number density, and volume fraction of the β″ and L precipitates summarized in Table 4, the contributions of different strengthening mechanisms to the yield strength were evaluated using the aforementioned models, as shown in Figure 12.

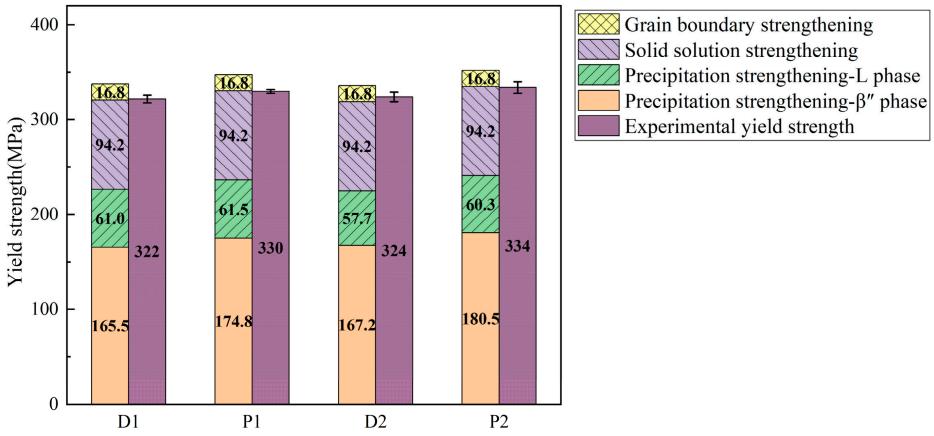


Figure 12. Comparison of the calculated and experimental yield strengths, along with the strengthening contributions of individual mechanisms, under different aging conditions.

As shown in Figure 12, precipitation strengthening plays a dominant role in the overall yield strength, while the contributions from solid-solution strengthening and intrinsic lattice strength can be considered essentially constant due to the identical alloy composition and solution-treatment procedures. Among the precipitates identified by TEM, β″ precipitates contribute more significantly to strengthening than L precipitates, primarily because they exhibit a much higher number density and larger volume fraction despite their smaller size. According to the shearable-precipitate strengthening model, the high spatial density of fine β″ precipitates effectively increases the frequency of dislocation–precipitate interactions, resulting in a greater cumulative strengthening effect. In contrast, the needle-like L precipitates are generally treated as non-shearable obstacles and their strengthening contribution

is described by the Orowan bypass mechanism; although individual L precipitates can strongly impede dislocation motion due to their larger size, their relatively low number density thus limits their overall strengthening contribution. Therefore, the strengthening-model calculations indicate that β″ precipitates are the primary strengthening phase in the present alloy, while the contribution from the L phase is comparatively limited.

Under the DA path, variations in room-temperature storage time do not lead to significant changes in the size or number density of either β″ or L precipitates, and the corresponding precipitation-strengthening contributions remain nearly constant, indicating that short-term room-temperature storage has only a limited influence on precipitate evolution during subsequent artificial aging and thus only a weak effect on the strengthening response. Although natural aging can influence the subsequent artificial-aging response in Al-Mg-Si(-Cu) alloys, and some clusters formed during natural aging may be unfavorable for β″ precipitation, this effect is closely related to the storage duration and cluster-evolution stage [43]. In the present work, the storage time of 6–48 h may only induce limited clustering evolution before final artificial aging, and the final aging treatment at 170 °C further promotes β″/L precipitation, weakening the subtle differences caused by short-term room-temperature storage. Therefore, both the mechanical properties and precipitation behavior show only limited sensitivity to room-temperature storage time within the investigated range. Under the PDA path, the precipitation-strengthening contributions from both β″ and L phases are generally higher than those under the DA path, with a particularly pronounced increase in the contribution from the β″ phase, demonstrating that pre-aging effectively enhances the efficiency of precipitation strengthening. Combined with TEM observations, it can be inferred that pre-β″ and pre-L clusters formed during pre-aging at 120 °C provide a larger number of effective nucleation sites for subsequent artificial aging at 170 °C, thereby increasing the number density of precipitates. Previous studies have shown that pre-aging can promote the formation of favorable clusters or β″-related precursor structures, which are more effective for subsequent β″ nucleation than some clusters formed during natural aging [23]. These pre-existing precursor structures are relatively stable during short-term room-temperature storage, so extending the storage time from 6 h to 48 h does not markedly change the final precipitate population or mechanical properties, and since the average precipitate size remains nearly unchanged, the enhancement in strengthening mainly originates from the increased precipitate number density [44].

Although the apparent sensitivity of mechanical properties to short-term room-temperature storage is not significant for either the DA or PDA paths, the underlying mechanisms differ fundamentally. For the DA path, room-temperature storage after solution quenching corresponds to a natural aging process, during which low-temperature stable clusters dominated by Mg-Si atoms are formed [20]. While these clusters exhibit a certain degree of thermal stability, they are inefficient in transforming into highly strengthening β″ precipitates during subsequent artificial aging. Instead, they consume solute atoms and vacancies that would otherwise participate in high-temperature precipitation, resulting in a reduced nucleation rate and limited number density of precipitates during artificial aging, ultimately weakening the precipitation-strengthening potential [45]. This mechanism explains the relatively lower strengthening contribution from the β″ phase observed under the DA path.

The PDA path modifies the initial precipitation pathway by introducing a controlled pre-aging treatment prior to artificial aging. Pre-aging at an appropriate temperature promotes the formation of inheritable precursor clusters (such as pre-β″ and pre-L), whose structure and composition are more closely related to those of the stable precipitates. Consequently, these clusters can more readily transform into β″ or L phases during subsequent

artificial aging. Although such precursor clusters exert only a weak direct obstacle effect on dislocation motion, they serve as highly efficient nucleation sites, leading to a substantial increase in precipitate number density. From a strengthening-mechanism perspective, the increased number density of β″ precipitates enhances the frequency of dislocation-precipitate interactions and is therefore reflected as a higher strengthening contribution in the model calculations.

In addition, the PDA treatment suppresses the formation of deleterious natural-aging clusters and improves the microstructural stability of the alloy during room-temperature storage [27]. The precursor clusters formed during pre-aging exhibit relatively high thermal and structural stability over short time scales; thus, even after a certain duration of room-temperature storage, their influence on subsequent artificial-aging precipitation behavior remains limited. This explains why both the mechanical properties and precipitation-strengthening contributions under the PDA path remain stable with extended room-temperature storage.

Overall, the effects of DA and PDA paths on alloy strengthening are not only reflected in differences in precipitate size or number density, but more fundamentally in their regulation of precipitation nucleation pathways and solute-evolution behavior. By optimizing the initial nucleation state, PDA increases the probability of forming effective strengthening precipitates and enhances strengthening efficiency, thereby enabling superior overall strength improvement.

Although the PDA route introduces an additional pre-aging step, the approximately 10 MPa increase in yield strength and ultimate tensile strength indicates that pre-aging can still improve the precipitation-strengthening response after short-term room-temperature storage. However, this improvement should be regarded as an initial laboratory-scale result rather than an optimized industrial process. The present pre-aging condition was not systematically optimized, and further improvement may be achieved by adjusting the pre-aging temperature, pre-aging time, room-temperature storage duration, and final artificial-aging parameters. From an industrial perspective, the practical significance of PDA treatment should be evaluated by balancing the additional processing cost against the potential strengthening benefit. For 6xxx Al alloys, intermediate storage or natural aging before final artificial aging can significantly influence the subsequent age-hardening response and may reduce the peak-aged strength in some alloys [11]. Therefore, the PDA route may be valuable as a potential strategy to mitigate the negative effect of room-temperature storage and enhance precipitation strengthening, although further process optimization and cost–benefit assessment are required before industrial implementation.

5. Conclusions

In this study, the precipitation pathway and strengthening response of an Al-Mg-Si-Cu alloy were compared under delayed artificial aging (DA) and pre-aging-assisted delayed artificial aging (PDA) routes. The conclusions are refined as follows:

- The 120 °C/1 h PDA treatment improved the mechanical properties of the Al-Mg-Si-Cu alloy after short-term room-temperature storage. Compared with the DA route, PDA increased both the yield strength and ultimate tensile strength by approximately 10 MPa after 6–48 h of room-temperature storage, with only a slight decrease in elongation. In contrast, extending the pre-aging time to 3 h was less beneficial, indicating that excessive pre-aging weakens the subsequent strengthening response.
- PDA significantly reduced the apparent activation energy for β″ precipitation and promoted the subsequent aging response. The apparent activation energy decreased from 107.13 kJ/mol in the solution-treated state and 102.74 kJ/mol in the DA-pre condition

to 70.63 kJ/mol in the PDA-pre condition, indicating that 120 °C pre-aging provides a more favorable precursor state for β″ precipitation during final artificial aging.

- The strengthening effect of PDA mainly originated from the increased number density of β″ precipitates rather than changes in precipitate size. Quantitative TEM results showed that PDA caused little change in the average sizes of β″ and L precipitates, while the number density of β″ precipitates increased by approximately 15% compared with the corresponding DA samples. Strengthening-model calculations confirmed that β″ precipitates dominate the precipitation strengthening contribution, whereas the contribution of the L phase accounts for only about 25%.

Author Contributions: Conceptualization, Q.Z., H.L., Y.T., Z.Z. and G.Q.; Methodology, H.J., Y.T., M.Y., Z.Z. and G.Q.; Validation, H.J. and G.N.; Formal analysis, G.N. and M.Y.; Investigation, Q.Z., Y.T. and G.N.; Resources, M.Y.; Data curation, Q.Z.; Writing—original draft preparation, Q.Z.; Writing—review and editing, X.G. and H.L.; Supervision, X.G., G.Q. and H.L.; Funding acquisition, Z.Z., G.Q. and H.L. All authors have read and agreed to the published version of the manuscript.

Funding: This research was funded by National key R & D projects, grant number No. 2023YFB3710902.

Data Availability Statement: The original contributions presented in this study are included in the article. Further inquiries can be directed to the corresponding author.

Acknowledgments: During the preparation of this work, the authors used ChatGPT (version 5.6, OpenAI) in order to improve the readability and language of the manuscript. After using this tool, the authors reviewed and edited the content as needed and take full responsibility for the content of the published article.

Conflicts of Interest: Hutian Li, Qingyong Zheng, Huixue Jiang, Yuxing Tian, Guanmei Niu and Mingchao Yu were employed by Chinalco Materials Application Research Institute Co., Ltd. The remaining authors declare that the research was conducted in the absence of any commercial or financial relationships that could be construed as a potential conflict of interest.

References

1. Zang, R.; Ding, L.; Ehlers, F.J.H.; Jia, Z.; Xu, S.; Li, Y.; Cao, L. The influence of Cu content and Mg/Si ratio on the strength and formability in Al-Mg-Si-Cu alloys. *Mater. Charact.* **2023**, *205*, 113355. [CrossRef]
2. Li, Y.; Wu, Z.; Wang, D.; Nagaumi, H.; Zhang, G.; Feng, Z.; Luo, X.; Luo, Y.; Zhang, H.; Zhang, B. Synergistic enhancement of strength and bendability of Al-Mg-Si-Cu alloys for safety components by adding Mn. *Mater. Des.* **2025**, *249*, 113531. [CrossRef]
3. Li, J.; Gao, M.; Yang, L.; Shen, C.; Guan, R. Effect of cold drawing on the microstructure and property of precipitation strengthening Al–Mg–Si–Cu alloy prepared by continuous casting-extrusion. *Mater. Sci. Eng. A* **2025**, *922*, 147669. [CrossRef]
4. Ding, L.; Jia, Z.; Nie, J.-F.; Weng, Y.; Cao, L.; Chen, H.; Wu, X.; Liu, Q. The structural and compositional evolution of precipitates in Al-Mg-Si-Cu alloy. *Acta Mater.* **2018**, *145*, 437–450. [CrossRef]
5. Wang, X.; Guo, M.; Cao, L.; Luo, J.; Zhang, J.; Zhuang, L. Effect of heating rate on mechanical property, microstructure and texture evolution of Al–Mg–Si–Cu alloy during solution treatment. *Mater. Sci. Eng. A* **2015**, *621*, 8–17. [CrossRef]
6. Wang, X.; Embury, J.D.; Poole, W.J.; Esmaeili, S.; Lloyd, D.J. Precipitation strengthening of the aluminum alloy AA6111. *Metall. Mater. Trans. A* **2003**, *34*, 2913–2924. [CrossRef]
7. Yuan, S.P.; Liu, G.; Wang, R.H.; Zhang, G.-J.; Pu, X.; Sun, J.; Chen, K.-H. Effect of precipitate morphology evolution on the strength–toughness relationship in Al–Mg–Si alloys. *Scr. Mater.* **2009**, *60*, 1109–1112. [CrossRef]
8. Wu, P.; Song, K.; Liu, F. Effect of coherent nanoprecipitate on strain hardening of Al alloys: Breaking through the strength-ductility trade-off. *Materials* **2024**, *17*, 4197. [CrossRef] [PubMed]
9. Jeong, W.; Yang, J.; Choi, J.P.; Hwang, J.Y.; Kim, Y.W.; Park, S.J.; Choi, J.W.; Heogh, W.; Lee, H.; Park, J.; et al. Al-based functionally graded super-intermetallic compounds for the turbine blade of a high-performance jet engine. *Adv. Compos. Hybrid Mater.* **2025**, *8*, 420. [CrossRef] [PubMed]
10. Boczkal, S.; Korczak, P.; Żyłka, K.; Limanówka, K.; Płonka, B.; Remsak, K.; Szymański, W.; Leśniak, D. Effects of copper content and thermo-mechanical treatment on microstructure and mechanical properties of AlMgSi(Cu) alloys. *Crystals* **2024**, *14*, 1027. [CrossRef]
11. Hell, C.M.; Søreide, H.-S.; Bjørge, R.; Marioara, C.D.; Li, Y.; Holmestad, R. Influence of natural aging and ramping before artificial aging on the microstructure of two different 6xxx alloys. *J. Mater. Res. Technol.* **2022**, *21*, 4224–4240. [CrossRef]

12. Guo, M.X.; Zhang, Y.D.; Li, G.J.; Jin, S.B.; Sha, G.; Zhang, J.S.; Zhuang, L.Z.; Lavernia, E.J. Solute clustering in Al-Mg-Si-Cu-(Zn) alloys during aging. *J. Alloys Compd.* **2019**, *774*, 347–363. [CrossRef]
13. Wang, Y.; Chen, J.; Nordlien, J.H.; Røyset, J.; Sunde, J.K.; Mørtsell, E.A.; Zhou, X. The formation of L-phase precursor originated from Cu-containing Guinier–Preston zone in Al–Mg–Si–(Cu) alloys. *Metall. Mater. Trans. A* **2026**, *57*, 3251–3266. [CrossRef]
14. Kawahara, Y.; Marioara, C.D.; Hell, C.M.; Thrane, E.S.; Mørtsell, E.A.; Røyset, J.; Holmestad, R.; Kaneko, K. Effect of Cu addition on atomic clusters and its influence on the dispersion of precipitates in Si-rich Al-Mg-Si alloys. *Mater. Sci. Eng. A* **2025**, *946*, 149121. [CrossRef]
15. Resch, L.; Klinser, G.; Hengge, E.; Enzinger, R.; Luckabauer, M.; Sprengel, W.; Würschum, R. Precipitation processes in Al–Mg–Si extending down to initial clustering revealed by the complementary techniques of positron lifetime spectroscopy and dilatometry. *J. Mater. Sci.* **2018**, *53*, 14657–14665. [CrossRef]
16. Cao, L.; Rometsch, P.A.; Couper, M.J. Clustering behaviour in an Al–Mg–Si–Cu alloy during natural ageing and subsequent under-ageing. *Mater. Sci. Eng. A* **2013**, *559*, 257–261. [CrossRef]
17. Yeh, C.-W.; Chen, C.-J.; Tai, C.-L.; Yang, Y.-L.; Misra, R.D.K.; Hsiao, C.-N.; Chen, C.-C.; Tsao, C.-S.; Jeng, U.S.; Lin, H.-C.; et al. Pre-aged and paint-baked strengthening response on the prolonged natural-aged Al-Mg-Si-Cu aluminum alloys. *J. Alloys Compd.* **2024**, *1008*, 176677. [CrossRef]
18. Saito, G.; Sano, Y.; Mizuno, K.; Torigoe, S.; Takata, K.; Okajima, T.; Muto, S. Precipitation behavior during low-temperature aging in Al–Mg–Si alloy using STEM-EDS intensity correlograms. *Mater. Sci. Eng. A* **2025**, *923*, 147686. [CrossRef]
19. Yang, Z.; Banhart, J. Natural and artificial ageing in aluminium alloys—The role of excess vacancies. *Acta Mater.* **2021**, *215*, 117014. [CrossRef]
20. Li, C.; Marioara, C.D.; Hatzoglou, C.; Andersen, S.J.; Holmestad, R.; Li, Y. Accelerating precipitation hardening by natural aging in a 6082 Al-Mg-Si alloy. *Acta Mater.* **2024**, *281*, 120396. [CrossRef]
21. Marioara, C.D.; Andersen, S.J.; Hell, C.; Frafjord, J.; Friis, J.; Bjørge, R.; Ringdalen, I.G.; Engler, O.; Holmestad, R. Atomic structure of clusters and GP-zones in an Al-Mg-Si alloy. *Acta Mater.* **2024**, *269*, 119811. [CrossRef]
22. Liu, T.; Scholtz, J.; Xue, F.; Yung, A.; Guiglionda, G.; Marquis, E.A. Effects of Cu and pre-aging on the clustering behavior in Al-Mg-Si alloys. *Materialia* **2023**, *32*, 101917. [CrossRef]
23. Zang, R.; Wan, B.; Ding, L.; Ehlers, F.J.H.; Jia, Z.; Cao, L.; Li, Y. The combined effect of pre-aging and Mg/Si ratio on the natural aging and bake hardening in Al-Mg-Si-0.7Cu alloys. *Mater. Charact.* **2024**, *212*, 113987. [CrossRef]
24. Ding, L.; He, Y.; Wen, Z.; Zhao, P.; Jia, Z.; Liu, Q. Optimization of the pre-aging treatment for an AA6022 alloy at various temperatures and holding times. *J. Alloys Compd.* **2015**, *647*, 238–244. [CrossRef]
25. Birol, Y. Pre-aging to improve bake hardening in a twin-roll cast Al–Mg–Si alloy. *Mater. Sci. Eng. A* **2005**, *391*, 175–180. [CrossRef]
26. *GB/T 16865-2023*; Test Pieces and Methods for Tensile Test for Wrought Aluminium, Magnesium and Their Alloy Products. Standards Press of China: Beijing, China, 2023.
27. Murayama, M.; Hono, K. Pre-precipitate clusters and precipitation processes in Al–Mg–Si alloys. *Acta Mater.* **1999**, *47*, 1537–1548. [CrossRef]
28. Gong, W.; Xie, M.; Zhang, J. Giant bake hardening response of multi-scale precipitation strengthened Al-Mg-Si-Cu-Zn alloy via pre-aging treatments. *Mater. Charact.* **2021**, *181*, 111464. [CrossRef]
29. Zhu, L.; Guo, M.; Zhang, J. Effect of silicon content on nucleation and growth of multiscale precipitates in Al–Mg–Si–Cu–Zn alloys for different aging paths. *Mater. Sci. Eng. A* **2022**, *841*, 143016. [CrossRef]
30. Torsæter, M.; Lefebvre, W.; Marioara, C.D.; Andersen, S.J.; Walmsley, J.C.; Holmestad, R. Study of intergrown L and Q′ precipitates in Al–Mg–Si–Cu alloys. *Scr. Mater.* **2011**, *64*, 817–820. [CrossRef]
31. Ghosh, K.S.; Gao, N. Determination of kinetic parameters from calorimetric study of solid state reactions in 7150 Al-Zn-Mg alloy. *Trans. Nonferrous Met. Soc. China* **2011**, *21*, 1199–1209. [CrossRef]
32. Guo, M.X.; Zhang, Y.; Zhang, X.K.; Zhang, J.S.; Zhuang, L.Z. Non-isothermal precipitation behaviors of Al-Mg-Si-Cu alloys with different Zn contents. *Mater. Sci. Eng. A* **2016**, *669*, 20–32. [CrossRef]
33. Kumar, M.; Poletti, C.; Degischer, H.P. Precipitation kinetics in warm forming of AW-7020 alloy. *Mater. Sci. Eng. A* **2013**, *561*, 362–370. [CrossRef]
34. He, S.; Wang, J.; Zhang, D.; Wu, Q.; Kong, Y.; Du, Y. A first-principles study of the Cu-containing β″ precipitates in Al-Mg-Si-Cu alloy. *Materials* **2021**, *14*, 7879. [CrossRef] [PubMed]
35. Liu, S.H.; Pan, Q.L.; Huang, H.F.; Wang, J.; Li, D.G.; Ning, Z.X.; Wei, L.L. Effect of natural aging and pre-aging on microstructure evolution and strengthening ability of Al-Mg-Si alloy during age hardening. *Trans. Nonferrous Met. Soc. China* **2025**, *35*, 3578–3594. [CrossRef]
36. Guo, M.X.; Li, G.J.; Zhang, Y.D.; Sha, G.; Zhang, J.S.; Zhuang, L.Z.; Lavernia, E.J. Influence of Zn on the distribution and composition of heterogeneous solute-rich features in peak aged Al-Mg-Si-Cu alloys. *Scr. Mater.* **2019**, *159*, 5–8. [CrossRef]
37. Tsao, C.-S.; Chen, C.-Y.; Jeng, U.-S.; Kuo, T.-Y. Precipitation kinetics and transformation of metastable phases in Al–Mg–Si alloys. *Acta Mater.* **2006**, *54*, 4621–4631. [CrossRef]

38. Esmaeili, S.; Lloyd, D.J. Characterization of the evolution of the volume fraction of precipitates in aged AlMgSiCu alloys using DSC technique. *Mater. Charact.* **2005**, *55*, 307–319. [CrossRef]
39. Nandy, S.; Ray, K.K.; Das, D. Process model to predict yield strength of AA6063 alloy. *Mater. Sci. Eng. A* **2015**, *644*, 413–424. [CrossRef]
40. Deschamps, A.; Brechet, Y. Influence of predeformation and ageing of an Al–Zn–Mg alloy—II. Modeling of precipitation kinetics and yield stress. *Acta Mater.* **1998**, *47*, 293–305. [CrossRef]
41. Esmaeili, S.; Lloyd, D.J.; Poole, W.J. A yield strength model for the Al-Mg-Si-Cu alloy AA6111. *Acta Mater.* **2003**, *51*, 2243–2257. [CrossRef]
42. Hornbogen, E.; Starke, E.A., Jr. Overview no. 102 Theory assisted design of high strength low alloy aluminum. *Acta Metall. Mater.* **1993**, *41*, 1–16. [CrossRef]
43. Kim, J.; Kobayashi, E.; Sato, T. Influence of natural aging time on two-step aging behavior of Al-Mg-Si(-Cu) alloys. *Mater. Trans.* **2015**, *56*, 1771–1780. [CrossRef]
44. Bahrami, A.; Miroux, A.; Sietsma, J. An age-hardening model for Al-Mg-Si alloys considering needle-shaped precipitates. *Metall. Mater. Trans. A* **2012**, *43*, 4445–4453. [CrossRef]
45. Ivanov, R.; Deschamps, A.; De Geuser, F. Clustering kinetics during natural ageing of Al-Cu based alloys with (Mg, Li) additions. *Acta Mater.* **2018**, *157*, 186–195. [CrossRef]

Disclaimer/Publisher's Note: The statements, opinions and data contained in all publications are solely those of the individual author(s) and contributor(s) and not of MDPI and/or the editor(s). MDPI and/or the editor(s) disclaim responsibility for any injury to people or property resulting from any ideas, methods, instructions or products referred to in the content.